Attosecond coherent control of oxygen dissociation by XUV-IR laser fields using three-dimensional momentum imaging

P. Ranitovic*
Chemical Sciences Division, Lawrence Berkeley National Laboratory, Berkeley, California 94720, USA and Laboratorium für Physikalische Chemie, ETH Zürich, 8093 Zürich, Switzerland

F. P. Sturm
Institut für Kernphysik, Universität Frankfurt, Max-von-Laue Strasse 1, D-60438 Frankfurt, Germany and Chemical Sciences Division, Lawrence Berkeley National Laboratory, Berkeley, California 94720, USA

X. M. Tong
Center for Computational Sciences, Tsukuba University, Tsukuba, Ibaraki 305-8577, Japan

T. W. Wright, D. Ray, I. Zalyubovskya, N. Shivaram, and A. Belkacem
Chemical Sciences Division, Lawrence Berkeley National Laboratory, Berkeley, California 94720, USA

D. S. Slaughter and Th. Weber
Chemical Sciences Division, Lawrence Berkeley National Laboratory, Berkeley, California 94720, USA

(Received 10 April 2018; published 16 July 2018)

We have performed ultrafast three-dimensional ion momentum imaging spectroscopy on the dissociative single ionization of oxygen molecules using attosecond pulse trains with a broad energy spectrum of 5–30 eV. High-resolution momentum imaging allows clear identification of vibrational structures corresponding to the predissociation of highly excited cationic states. By adding a pump infrared field that is synchronized with and polarized orthogonally to the XUV pulse train, and an additional probe IR field, we demonstrate how the yield of O^+ ions can be steered between different dissociation channels by coherently controlling the coupling between multiple O_2^{+*} electronic states on an attosecond time scale. Time-dependent calculations in a single active electron approximation allow a qualitative analysis of ion yields for two orientations of the molecular axis.

DOI: 10.1103/PhysRevA.98.013410

I. INTRODUCTION

Precise control of photochemical reactions requires a clear understanding of coupled electronic and nuclear motion and has been a pursuit of the ultrafast science community since the field of femtochemistry was established [1]. While femtosecond (fs) pulsed lasers allow for tracing the temporal evolution of the molecular nuclear motion [2], the electron dynamics develops on an even shorter, attosecond (as), time scale, and can be probed using a combination of isolated attosecond pulses and a near-infrared (IR) laser field, as demonstrated by attosecond streaking techniques [3], or by the measurement of the tunneling time in strong-field ionization [4]. On the other hand, attosecond pulse trains (APTs), created by high-order-harmonic generation (HHG) sources, have a broad bandwidth and spectrally well-defined individual harmonics. When combined with synchronized IR pulses, control of ultrafast processes in molecules can be achieved, allowing extension of attosecond quantum coherent control processes to the extreme ultraviolet (XUV) spectral region [5,6].

The concept of temporal coherent control of interfering quantum pathways by optical fields was introduced by Brumer and Shapiro [7], and demonstrated with femtosecond pulses in cesium by Blanchet *et al.* [8], and in molecules by Gordon *et al.* [9]. In these early experiments, the optical field was used to couple ground electronic states to the same final state by means of two-pathway interference processes. The resulting interference of the different pathways exhibits a phase-modulated probability of reaching the final state. The coherent control concepts were extended to the XUV regime in the experiments where high harmonic laser pulses were combined with an infrared field to coherently control the ionization in helium [5,6], or to induce electromagnetic transparency by controlling the amplitudes of the XUV harmonics [10]. More recently, the two-pathway electron wave-packet interference was applied to coherently control the double-ionization yield in argon [11]. The ultrashort duration of the XUV and IR pulses allowed the extrapolation of the attosecond coherent control concepts to the non-Born-Oppenheimer regime where the electron wave-packet interference is influenced by the nuclear wave-packet motion. This was demonstrated in highly excited molecules such as oxygen and deuterium [12,13].

In previous experiments [14–17], a strong infrared field was used to control the ionization and dissociation of small molecules such as oxygen and to study the dynamics induced in the laser dressed system. By using a combination of spectrally

*pranitovic@lbl.gov

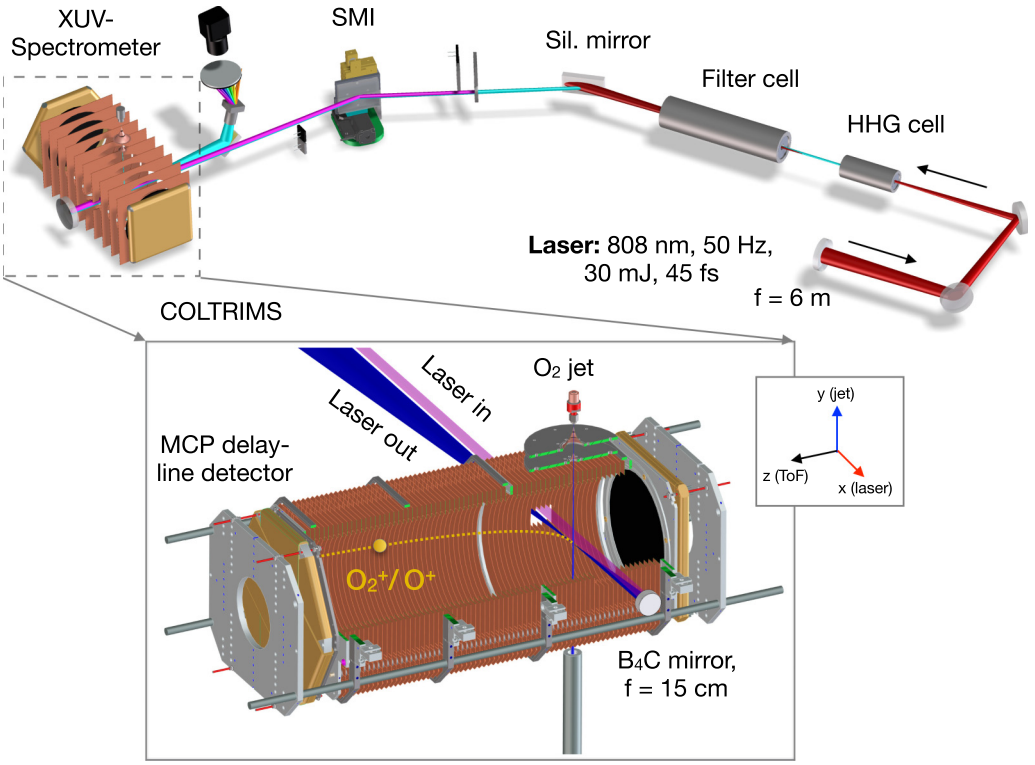

FIG. 1. Top: Beamline for generating high flux high harmonic laser pulses using a high power infrared laser system with a loose focusing geometry. The split-mirror interferometer (SMI) splits the XUV and IR beam and provides an adjustable delay between the pump and probe pulses. Bottom: The sketch shows the COLTRIMS style spectrometer used for 3D momentum imaging of the ion fragments. Note the small inset which introduces the laboratory coordinate frame, with the x direction representing the XUV and IR light propagation, the y axis being the jet and IR polarization direction, and z corresponding to the time of flight and XUV polarization direction.

selected high harmonics and a strong laser field, the steering of the dissociative ionization can be controlled for specific electronic states [18–21].

In this work, we investigate the dissociation pathways of oxygen molecules populated by attosecond XUV pulse trains in the range of 5–30 eV. In order to control the dissociative ionization of O_2^{+*}, we employ two IR pulses where the first pulse is phase locked to and temporally overlapped with the XUV pulse, while the second IR pulse is delayed with attosecond precision. To systematically study the processes at hand, we first analyze the case when the XUV pulse acts alone, and we compare the O^+ yields along and perpendicular to the XUV polarization for several dissociative limits of O_2^+, in a non-time-resolved manner. We identify dissociation channels by their asymptotic final states and compare our results with previous work on this molecule. Then we analyze the influence of an IR field on the ion spectra, measured via high-resolution three-dimensional (3D) ion-momentum imaging, where vibrational structures in the O^+ yield are observed as a function of kinetic energy, permitting the investigation of near-threshold dissociation with great detail. Finally, the effects of optical interference of the two IR pulses and the quantum interference of the electronic states (excited by the XUV harmonics and recombined by the IR field) are investigated by observing the total ion yield changes in a time-resolved way for different orientations of the molecular axis with respect to the linear polarization of the XUV beam. A coherent superposition of electronic states is created by a comb of XUV harmonics exciting the target, and the resulting coherent electronic wave-packet dynamics is modulated in a controlled manner by the IR pulses. The resultant interference is observed in the time-dependent fragment and parent ion yields for specific molecular orientations relative to the XUV and IR polarization. We find that the total O_2^+ and O^+ yields can be modulated, and that the predissociation process is sensitive to the phase variation between the XUV and IR pulses. A qualitative interpretation of the experimental results is aided by single-active-electron time-dependent Schrödinger equation calculations.

II. EXPERIMENTAL SETUP

We show a schematic of the experimental setup in Fig. 1. We have combined a high-power IR laser system (808 nm, 30 mJ, 45 fs, 50 Hz) with a beamline for the generation, selection, and characterization of extreme ultraviolet (XUV) pulses using high-order-harmonic generation (HHG). We loosely focus ($f = 6$ m) the infrared pulses into a gas filled cell to efficiently generate VUV and XUV pulses with ~15-fs pulse duration. The pulse duration was approximated from the bandwidth of the harmonics, and it was found that the pulse can be as short as 6 fs. The typical pulse duration that we get from the cross-correlation measurements is up to 15 fs. Downstream from the HHG source two mirrors at Brewster angle suppress the horizontally polarized component of the IR pulses by a factor of $\sim 10^6$, and only let the vertically polarized contribution pass through, while the horizontally

polarized XUV pulses are reflected with 80% efficiency. The copropagating XUV and IR pulses are split into pump and probe arms using a custom-built split-mirror interferometer with 200 as resolution. The IR beam in the pump arm is intrinsically phase locked to the XUV beam by the very nature of the HHG process, whereas the IR beam in the probe arm can be delayed with respect to the beams in the pump arm. The IR pulses in both arms are orthogonally polarized to the XUV beam. The diverging pump and probe beams miss the target on their first pass through the cold-target recoil-ion momentum spectroscopy (COLTRIMS) spectrometer, and are backfocused into a supersonic molecular gas jet of oxygen molecules by a curved mirror ($f = 15$ cm) inside the spectrometer. A B_4C coating on the backfocusing mirror reduces the reflected XUV spectrum to the energy range of ~5–30 eV. Electronically excited dissociating molecular O_2^+ ions were analyzed with a state-of-the-art COLTRIMS type 3D momentum imaging spectrometer. A homogeneous electric field guides the ions onto a time and position sensitive detector consisting of multichannel-plates (MCPs) with delay-line readout [22]. The 3D ion momenta at the instant of dissociation can be reconstructed from the times of flight and the positions of impact of the particles to and on the detector. A detailed description of the XUV beamline and the momentum imaging end station can be found in a separate publication [23].

III. EXPERIMENTS

A. Dissociative single ionization of oxygen molecules

In all the experiments presented here, we have ionized oxygen molecules in the ground state with a spectrum of high harmonic laser pulses ranging from ~5–30 eV energy. The potential-energy curves in the relevant XUV energy region are shown in Fig. 2. Several bound electronic states can be populated by photons of the 13th (20 eV) and 15th (23 eV) harmonic orders. The first dissociation limit of O_2^+ (L1) lies at 18.73 eV, thus no contribution to the spectrum of O^+ ions is expected from the 11th harmonic alone. The electronic states of the O_2^+ ion in the energy range of 19–26 eV are known to predissociate efficiently into a neutral oxygen atom and one oxygen ion through a nonadiabatic coupling with states in this region. The predissociation process happens on picosecond time scales making it possible for us to observe the vibrational structure of different electronically excited O_2^+ states in ion momentum and energy space. This effect has been studied using photoelectron spectroscopy [24,25], photoion spectroscopy [26], as well as coincidence photoelectron-photoion spectroscopy [27,28].

In the following discussion, our coordinate system is defined as follows: the z axis is parallel to the XUV polarization and the electric extraction field of the momentum spectrometer (i.e., time-of-flight direction). The y axis is parallel to the pump and probe IR polarization direction and along our supersonic gas jet. The x direction is along the XUV and IR light propagation direction. Figure 3(a) shows the ion momentum images in the x-z plane obtained from irradiating oxygen molecules with a selection of high harmonics (11th–15th) only. We also projected the momentum distribution to obtain the energy spectra in Fig. 3(b) for the total yield (integrated over all ion emission angles, black line), and the yield inside a cone along

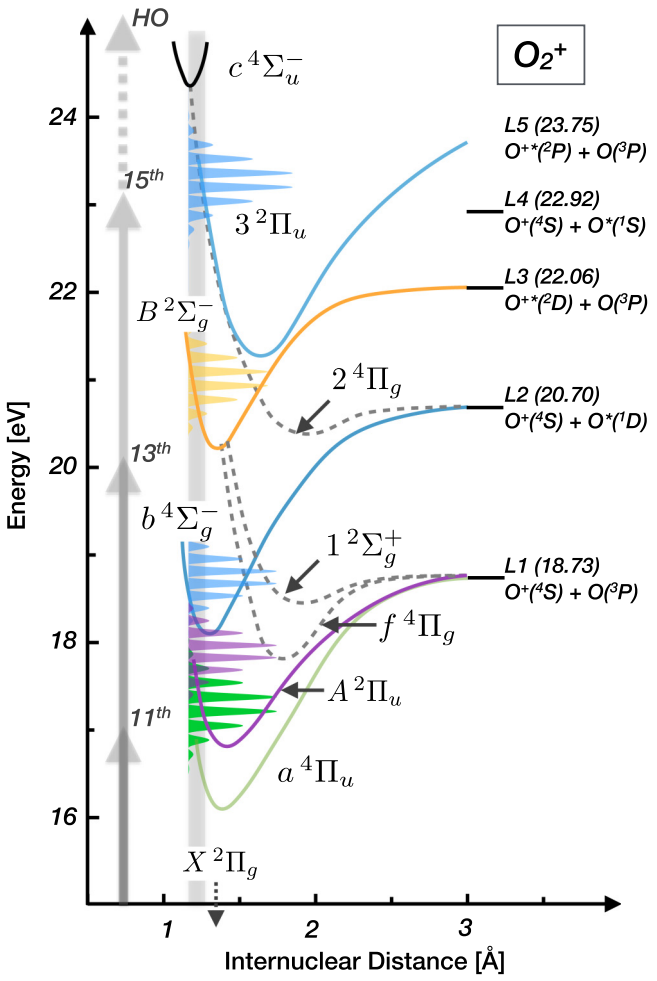

FIG. 2. Selected potential-energy curves of the molecular cation O_2^+ . The 11th (16.9 eV), 13th (20 eV), and 15th (23 eV) harmonics coherently populate several electronic states, as illustrated in the figure as vertical grey arrows. Nuclear-wave packets are created in several potential-energy curves in the Franck-Condon region (indicated by a vertical line at 1.25 Å), from where the molecular ion dissociates into several limits, labeled as L1–L5.

the z axis (blue line) where the O^+ kinetic energy is measured with the highest resolution (43-meV energy width at 0.8 eV; for details see [23]). By doing so, we observe several groups of peaks and label them with capital letters from A to D in the 1D energy spectrum. We first assign the peaks and then discuss how the IR modifies the peaks. Two series of sharp peaks, one at energies <0.3 eV (A), and one around 0.8 eV (C), dominate the spectrum. Lafosse *et al.* [29,30] identified some of the relevant transitions and dissociation mechanisms by a coincidence electron-ion 3D momentum measurement using a synchrotron light source. The present experiments reveal vibrational structures with a great level of detail. First, we will discuss the features generated solely by the XUV field (Fig. 3) before discussing the modifications induced by the infrared field. For the purpose of identification, we have classified the dissociation pathways using the roman numerals I–VII, sorted by the fragment kinetic energy.

The sharp peaks in region C of Fig. 3(b) correspond to the spacing of the vibrational progression of the $B\,^2\Sigma_g^-$ state of the

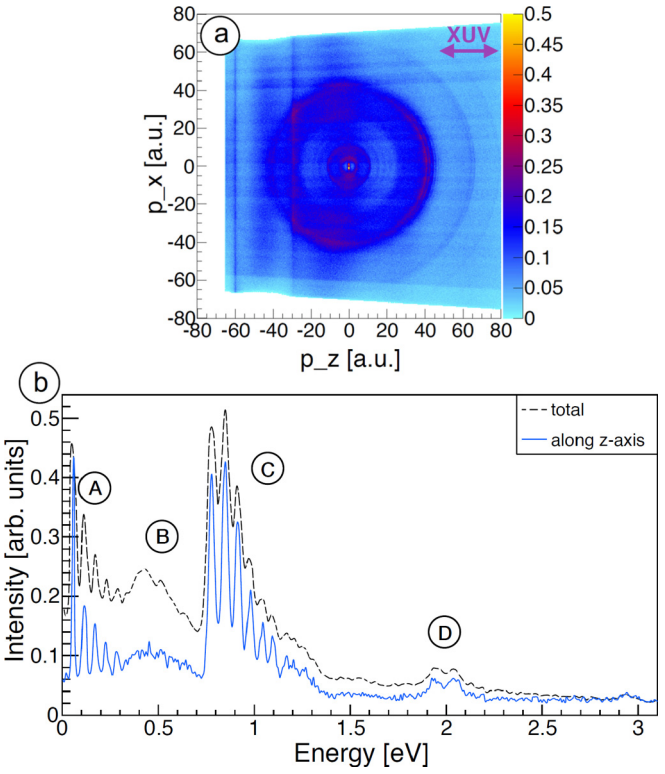

FIG. 3. (a) O^+ 2D ion momenta in the x-z plane after dissociation of O_2 molecules using XUV pulses only (16.9, 20, and 23 eV). (b) Kinetic energy of the O^+ ions after dissociation of O_2 molecules using XUV pulses only. The dashed line shows the result averaged over all molecular fragmentation angles with respect to the XUV polarization. The solid line represents the molecular breakup in a cone (with an open angle of 37°) along the XUV polarization axis (z axis, i.e., TOF axis). The letters A–D mark four different features discussed in the text. We note that the data here are analyzed in the p_z-p_x plane.

O_2^+ ion with the lowest level $v = 0$ at 20.296 eV and a spacing of 137 meV to the next vibrational state. This state dissociates into an O^+ ion, which is measured here, and a neutral oxygen atom. At the XUV energy of 23 eV, corresponding to the photon energy of the 15th harmonic, around 70% of the state is dissociated to the L1 limit at 18.73 eV (pathway *V*) by a nonadiabatic coupling (NAC) with the $f\,^4\Pi_g$, the $1\,^2\Sigma_g^+$, and the $d\,^4\Sigma_g^+$ state [27,29] which results in the peak series in region (C) of Fig. 3(b),

$$X\,^3\Sigma_g^- \xrightarrow{15\,\omega} B\,^2\Sigma_g^- + e^- \xrightarrow{NAC} 1\,^2\Sigma_g^+,\ f\,^4\Pi_g,\ d\,^4\Sigma_g^+ \xrightarrow{diss.} \mathrm{L1}. \quad \text{(V)}$$

Predissociation to the L2 limit at 20.70 eV via the $2\,^4\Pi_g$ state can occur starting at the $v = 4$ vibrational level (pathway *II*) but is less likely [27,29]. It leads to O^+ ion energies at 0.056 eV and higher as observed in region (A) of Fig. 3(b),

$$X\,^3\Sigma_g^- \xrightarrow{15\,\omega} B\,^2\Sigma_g^- + e^- \xrightarrow{NAC} 2\,^4\Pi_g \xrightarrow{diss.} \mathrm{L2}. \quad \text{(II)}$$

The $b\,^4\Sigma_g^-$ state has a similar vibrational structure as the $B\,^2\Sigma_g^-$ state and is mostly populated by the 13th harmonic. The vibrational state $v = 5$ with a binding energy of 18.847 eV [31], and the vibrational levels above it, predissociate to the L1 limit via the $f\,^4\Pi_g$ and the $d\,^4\Sigma_g^+$ states (pathway *I*) [29]. The resulting ion energies start at 0.059 eV and overlap with pathway *II* with less than 10 meV separation. Therefore, no clear assignment is possible without the coincident measurement of the photoelectron energy,

$$X\,^3\Sigma_g^- \longrightarrow 13\,\omega b\,^4\Sigma_g^- + e^- \xrightarrow{NAC} f\,^4\Pi_g,\ d\,^4\Sigma_g^+ \xrightarrow{diss.} \mathrm{L1}. \quad \text{(I)}$$

Note that both $B\,^2\Sigma_g^-$ and $b\,^4\Sigma_g^-$ originate from the same inner-shell $3\sigma_g$ single electron ionization with different final spins.

In region (B) of Fig. 3(b), from ion energies of 0.3 to 0.7 eV, a broad distribution peaking around 0.4 eV is observed. Several pathways are likely contributing to the O^+ ion energy spectrum. A variety of Rydberg states have been observed in the region of 20–26 eV that dissociate into neutral fragments followed by autoionization [24]. At 23 eV photon energy Lafosse *et al.* [29] identified the $3\,^2\Pi_u\ 4s\sigma_g$ Rydberg level as an important contribution to the O^+ ion fragments. This state dissociates into two neutral oxygen atoms with the configuration $O(^3P) + O^*(^2P,3d'')$ and autoionizes to the atomic states of the L3 limit (pathway *IV*). In the present experiments, the O^+ ion, created by an XUV photon energy of 23 eV (15th harmonic) has an energy of 0.4 eV, which is also broadened by the harmonic spectral bandwidth of (∼300 meV). We note here that the XUV pulse duration and the autoionization process are on the same femtosecond time scale. The 300-meV spectral bandwidth of the measured harmonics suggests an XUV pulse duration of approximately 15 fs,

$$X\,^3\Sigma_g^- \xrightarrow{15\,\omega} 3\,^2\Pi_u\ 4s\sigma_g \xrightarrow{diss.} O(^3P) + O^*(^2P,3d'') \xrightarrow{auto-ion.} L3 + e^-. \quad \text{(IV)}$$

Moreover, when the $3\,^2\Pi_u$ state of O_2^+ is populated in the Franck-Condon region with the 15th harmonic, it may dissociate directly to the adiabatically connected L3 limit at 22.06 eV (pathway *III*) [27]. This creates a broad O^+ ion spectrum centered at 0.5 eV (see also [25]),

$$X\,^3\Sigma_g^- \xrightarrow{15\,\omega} 3\,^2\Pi_u + e^- \xrightarrow{diss.} L3. \quad \text{(III)}$$

Further features are observed in the spectrum at 2 eV as well as at 3 eV O^+ ion energy. These peaks are generated from the predissociation of the $c\,^4\Sigma_u^-$ state of the O_2^+ ion. This state has a shallow potential well with two vibrational levels at 24.564 and 24.756 eV. Pathway *VI* corresponds to the predissociation into the L2 limit by tunneling [29] that produces the O^+ ion fragments at 1.93 and 2.03 eV. The $v = 0$ state also predissociates to the L1 limit with a fragment ion energy of 2.92 eV (pathway *VII*),

$$X\,^3\Sigma_g^- \xrightarrow{17\,\omega} c\,^4\Sigma_u^- + e^- \xrightarrow{diss.} L1, \quad \text{(VI)}$$

$$X\,^3\Sigma_g^- \xrightarrow{17\,\omega} c\,^4\Sigma_u^- + e^- \xrightarrow{diss.} L2. \quad \text{(VII)}$$

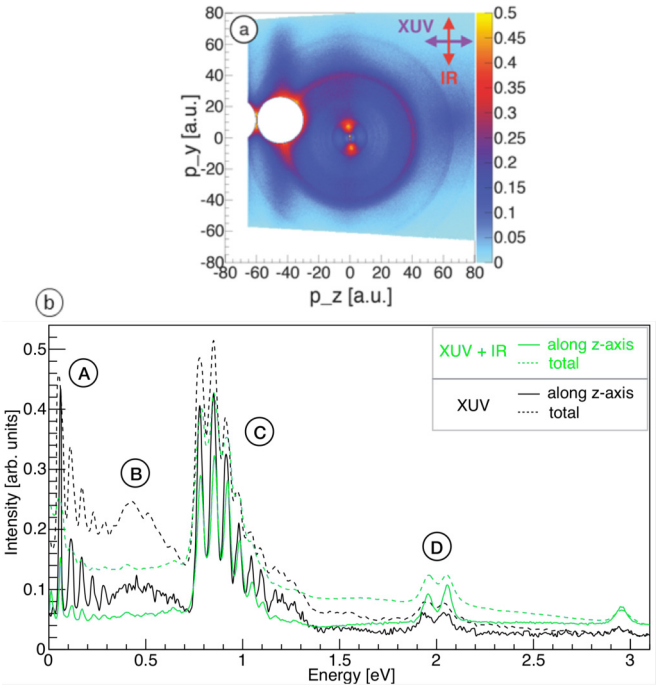

FIG. 4. (a) O^+ 2D ion momenta in the y-z plane after dissociation of O_2 molecules using XUV pulses (16.9, 20, and 23 eV) in the presence of the phase-locked orthogonal IR field in the pump arm. The contributions from stable OH^+ and H_2O^+ ions have been blocked out in this multipulse scheme only (white circles). (b) Kinetic energy of the O^+ ions after dissociation of O_2 molecules. The dark (black) solid and dashed lines show the kinetic energies of the O^+ using XUV pulses only [same as Fig. 3(b)]. The light (green) solid and dashed lines represent the data with the simultaneous action of the XUV and IR fields. The dashed lines show the result averaged over all fragmentation angles. The solid lines represent the molecular breakup in a cone (with an open angle of 37°) along the XUV polarization axis (z axis, i.e., TOF axis). The letters A–D mark four different features and are used in the discussion. We note that the data here are analyzed in the p_z-p_y plane and should not be directly compared with the data analyzed in the p_z-p_x plane due to the slightly different slicing conditions done in the analysis of Fig. 3.

Note that the $c\,^4\Sigma_u^-$ originates from the inner-shell $2\sigma_u$ single electron ionization.

B. Effects of IR assisted ionization

With the spectral features identified, we now turn to how the IR generally modifies the dissociative ionization processes, comparing the effects of the XUV and the probe IR fields on the 2D momentum and 1D energy spectra of the O^+ ion in Fig. 4 [black and blue lines in panel (b)]. While the spectrum in the presence of an IR field conserves the main features observed in the ionization using high harmonics only (black line), we see that the presence of the IR field significantly alters the XUV-induced dissociative ionization processes in different energy regions (blue line). The IR intensity was sufficient to ionize about one oxygen molecule per shot, corresponding to less than 20% of the total ionization rate. We estimate the IR intensity to be on the order of $\sim 5 \times 10^{13}$ W/cm^2. Several striking features are immediately recognizable: in the low-energy part of the

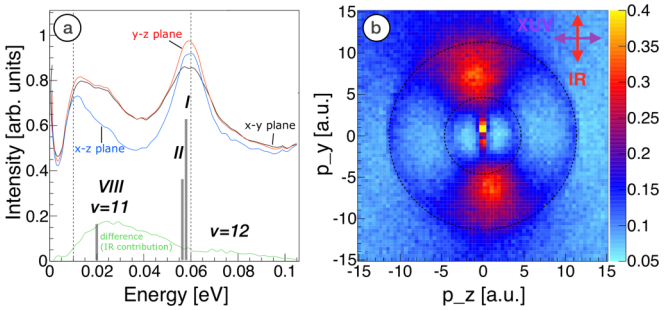

FIG. 5. (a) O^+ ion energies corresponding to different conical slices (collars with an open angle of 37°) in the (black) x-y momentum plane, i.e., where the XUV pulse is out of plane, (blue) x-z momentum plane, i.e., where the IR is out of plane, and (red) y-z momentum plane, i.e., where both XUV and IR are in plane. The difference (green) of (y-z plane)-(x-z plane) possibly removes most of the XUV-only contribution. (b) detailed view of the O^+ ion momentum distribution in the y-z momentum plane, i.e., where both XUV and IR are in plane.

spectrum (i.e., region B), as well as in the main dissociation channel (region C) the O^+ yield gets suppressed, while in the high-energy part of the spectrum (i.e., region D) the yield gets enhanced.

In more detail, in region D, around an oxygen ion energy of 2 eV and above, the peaks formed from the ionization to the $c\,^4\Sigma_u^-$ state have become stronger while the intensity of the ion yield in regions A–C, from 0.1–1.2 eV, has decreased with respect to the total yield. The increased population of the $c\,^4\Sigma_u^-$ state can be explained with the multiphoton excitation of the $c\,^4\Sigma_u^-$ state by simultaneous absorption of XUV and IR photons. Here the IR field couples the autoionizing states, excited by the 15th harmonic, to the $c\,^4\Sigma_u^-$ state by an absorption of one IR photon.

Another channel opens up in the presence of the IR field which is readily observable in the momentum spectra around 7 a.u. along the IR polarization axes, which corresponds to an energy value of 0.02 eV. In Fig. 5, we focus on the momenta and energies of the O^+ ions below 15 a.u. and 0.1 eV, respectively. In this low-energy region the ion field is suppressed by the IR field. The ultrahigh resolution of the setup reveals the features of just a few meV in the energy spectrum, as shown in Fig. 5(a). The y-z cut through the momentum sphere, as seen in Fig. 5(b), shows two isotropic sharp rings at 10 and 60 meV that are marked by dashed lines in the energy spectrum. The higher energy peak was already identified in the XUV-only measurement. It corresponds to the dissociation pathways *I* and *II*: the predissociation of vibrational level $v = 4$ of the $b\,^4\Sigma_g^-$ state to limit L1, and the $B\,^2\Sigma_g^-$ state to limit L2, producing O^+ fragments with 57 and 56 meV energy, respectively.

The origin of the isotropic ion energy distribution with just 10 meV, corresponding to a circle with 4.5 a.u. radius in ion momentum as shown in Fig. 5(b), is less obvious to assign at this point. The only transition found with such low energy consists in the predissociation of the vibrational level $v = 6$ of the $3\,^2\Pi_u$ state to the dissociation limit L3. This would yield ion fragments with 5 meV energy. Coupling through many-electron states with $^2\Pi_u$ symmetry could enable the predissociation of this state (see Fig. 2 in [25]). The

discrepancy of 5 meV could be explained with the apparent shift of the calibration of about 2–3 meV, visible at the calculated and measured position of the identified processes *I* and *II*, as well as with the limit of the instrument resolution.

Figure 5(b) shows a broader momentum distribution oriented along the polarization direction of the IR beam between 4.5 and 10 a.u. This corresponds to the shoulder around 25 meV in the kinetic-energy spectra (black trace x-y) and (red trace y-z) of Fig. 5(a). Subtracting the spectrum where the XUV contribution is seen in the z direction while the IR polarization axis is excluded (i.e., momentum slice in the x-z plane, represented by the blue trace), from the spectrum where the XUV contribution is along the z direction, and the IR polarization contributes to the O^+ yields (i.e., momentum slice in the y-z plane, represented by the red trace), results in the isolation of the features contributed by the IR field along the IR polarization axis. This is represented by the green trace in the O^+ energy spectrum. This feature at 25 meV can be attributed to the IR enabled predissociation of high vibrational levels of the $a\,^4\Pi_u$ state, as reported in [16,32]. This multicolor-multiphoton process (XUV+IR) is comparable with the dissociation of the $1s\sigma_g$ ground state of an H_2^+ ion by infrared photon coupling to the dissociative potential of the $2p\sigma_u$ state [33]. In the present experiments on O_2, the vibrational level $v = 11$ of the $a\,^4\Pi_u$ cation state can be coupled to the $f\,^4\Pi_g$ state by one IR photon dressing, followed by the dissociation to the limit L1. The calculated fragment O^+ ion energy is 20 meV (corrected for 808 nm from [16]). The next vibrational level yields O^+ ions with ∼65 meV of kinetic energy.

$$X\,^3\Sigma_g^- \xrightarrow{13\,\omega} a\,^4\Pi_u + e^- \xrightarrow{NAC} f\,^4\Pi_g\,(-1\,\omega) \xrightarrow{diss.} \mathrm{L1}. \tag{VIII}$$

Another possible channel that can produce the low-energy O^+ ions predissociating to the L1 limit can stem from the population of the Π_u state by the 11th harmonic in the Franck-Condon region, which is subsequently coupled to the $b\,^4\Sigma_g^-$ by the additional absorption of one IR photon (i.e., see Fig. 6).

Another striking feature in the dissociation of oxygen molecules in the presence of an infrared field is the sharp and discrete peak at 0 eV ion energy, visible as a central spot in the momentum distribution of Fig. 5(b). Ions with zero kinetic energy have been observed in previous investigations of dissociative ionization of O_2 [12,15,16] but in each of those experiments the resolution of the fragment energy was insufficient to distinguish the sharp peak below 4 meV observed in the present experiments. One possible source of such zero kinetic-energy ions is the IR enabled population of vibrational states just above the dissociation barrier, which can dissociate directly. This process usually has a low probability, which is perhaps consistent with the 0.3% of the yield of the O^+ fragments in the range of 0–1.2-eV kinetic energy.

Alternatively, the zero kinetic energy ions could be stable O_2^{2+} dications that are indistinguishable from O^+ ions in the present experiment, due to their identical times of flight. The double ionization threshold of O_2^{2+} is 36.13 eV [34]. The recoil energy of an electron with maximal energy ∼2 eV on an O_2^{2+} ion is below 1 meV, therefore if dications are formed, they are expected to appear well within the O^+ zero kinetic-energy

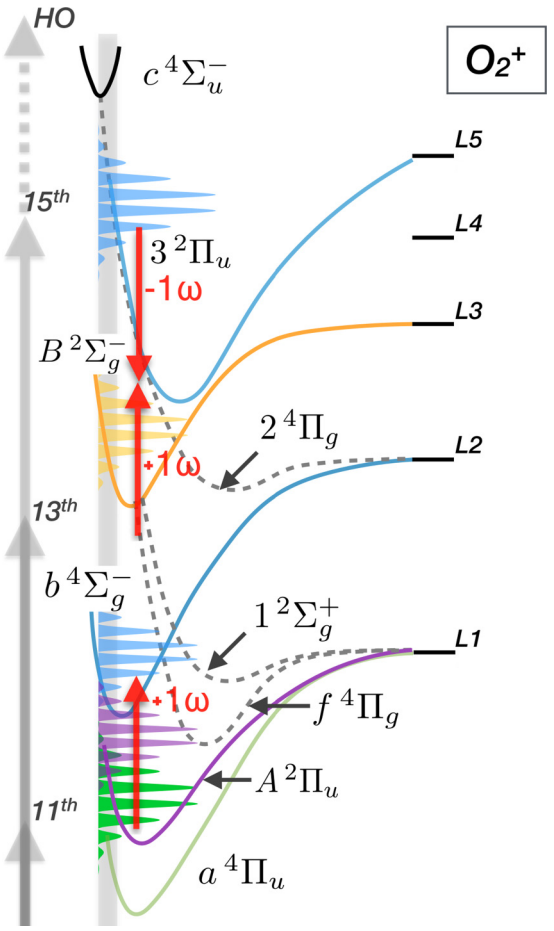

FIG. 6. Sketches of the selected oxygen cation potential-energy curves for IR-enabled couplings of electron and nuclear wave packets. The addition of an IR field can result in a two-pathway interference process of the electronic states populated by the 13th and 15th harmonics and coupled to the electronic state with an effective energy of the 14th harmonic by an absorption or emission of one IR photon from the IR laser field, as indicated by the +/− 1ω arrows. The $b\,^4\Sigma_g^-$ state can be populated by a multicolor or multiphoton absorption process (i.e., 11th + ω), as well as by direct absorption of the 13th harmonic.

feature. The 25th harmonic ($h\nu = 38.4$ eV) or a combination of the 23rd harmonic and one IR photon (36.8 eV) can populate the $X\,^1\Sigma_g^+$ ground state of the O_2^{2+} . Double ionization at this energy accounts for about ∼10% of the total ionization yield [35]. However, this number includes the autoionization of excited states above the $O^+(^4S) + O^+(^4S)$ dissociation limit at 32.35 eV, that dissociate into O^+ ions with large kinetic energy, a process that is known to play an important role but was not observed here [35]. Therefore, no clear conclusion can be given on the origin of ions producing the 4-meV feature.

C. Attosecond coherent control

Quantum and optical interference can be used to coherently control the population of different states and open new dissociation pathways on an attosecond time scale [12,13]. Splitting the infrared field into two arms and delaying each arm with respect to the other leads to optical interference of

the two IR beams once they are focused onto the target jet. This can be used to actively modulate the effective IR field strength the molecules experiences at the instant of the XUV pulse. For example, if the field strength is equal in both arms, $A = B$, the intensity of the IR field can be adjusted between zero and $|2A|^2$ by controlling the pump-probe delay. This effect is called *optical interference*, and it manifests itself in a modulation of the transition probability of an IR-assisted transition with frequency ω with respect to the pump-probe delay. When combined with the XUV field, the effects of the IR fields are nullified for the phase where the two IR fields interfere destructively, and maximized in the case of the constructive interference of the two IR fields. We note here that at each delay step of the split-mirror interferometer, the molecule experiences only one effective IR field. This field can result in the change of the XUV absorption probability. It can shift and broaden the electronic states, drive IR-assisted ionization of Rydberg states, or interrupt the autoionization of the states populated by the XUV pulse. Furthermore, the IR-enabled changes in the absorption probability of different XUV harmonics can contribute to the continuous change of the amplitudes of different interfering ionization channels, as the phase of the pump and probe pulses is scanned.

Quantum interference arises when an electronic state is coherently populated via two (or more) different quantum pathways. For example, this can be realized with high harmonic pulses when two electronic states are populated by the neighboring odd harmonics, e.g., $13\,\omega$ and $15\,\omega$, in the presence of an IR field, as shown in Fig. 6. In the Franck-Condon region, the state $B\,^2\Sigma_g^-$ is located energetically between intermediate electronic states accessed by the 13th and 15th harmonics. Two two-photon pathways, (i) $13\,\omega + \omega$ and (ii) $15\,\omega - \omega$, can lead to a population of the same electronic state $B\,^2\Sigma_g^-$ via intermediate electronic states, for example the $3\,^2\Pi_u$ state, and the $A\,^2\Pi_u$ state shifted up by 1ω due to the presence of the IR field in the pump arm of the experiment when the XUV interacts with the oxygen molecule. The quantum interference of the two pathways results in oscillations of the ionization probability at a frequency of $\sim 2\omega$, equivalent to the energy spacing of the coherently excited states that can be controlled by the relative delay between the XUV pulse and the IR fields. The amplitude of the total yield oscillation depends on the amplitudes of the two interfering pathways. For the case of a perfect match of the amplitudes, the IR field can completely transfer the populations of the states excited by the 13th and 15th harmonics to the new electronic state with the total two-photon energy of 14ω. On the other hand, when the quantum phase leads to a destructive interference of the two pathways, the IR field does not influence the initial population of the electronic states excited by the XUV pulse. Quantifying the amplitudes of each of the interfering pathways is far from trivial, especially in a molecule where the interplay of the nuclear and electronic wave packets plays a significant role.

The signal recorded in an experiment contains a convolution of optical interference at the frequency of the driving field ω, as well as quantum interference at the frequency $2\,\omega$, corresponding to the energy difference between the coupled states. Since the 45-fs IR pulses of the pump and probe arm of the experiment always overlap in our time delay interval, optical interferences cannot be separated from quantum interferences for this period. Nevertheless, while optical interference only appears at delays where the pump and the probe pulses overlap in time, quantum interference instead persists beyond the optical overlap, as long as both states are coherently excited and both pathways to the final state are enabled by the probe. A phase lag exists between the quantum oscillation and the XUV pulse that depends sensitively on the photon energy. By extracting this quantum phase between interfering electronic wave packets, information about the shape of the electronic potentials can be obtained [9]. In the case of a moderate to strong electromagnetic field, the modification of the electronic states by the IR field can be extracted from the phase, as shown by Shivaram *et al.* [36]. They also demonstrated how the optical interference of the infrared field can be used as a reference to measure the intensity dependent quantum phase between the oscillations of the quantum paths.

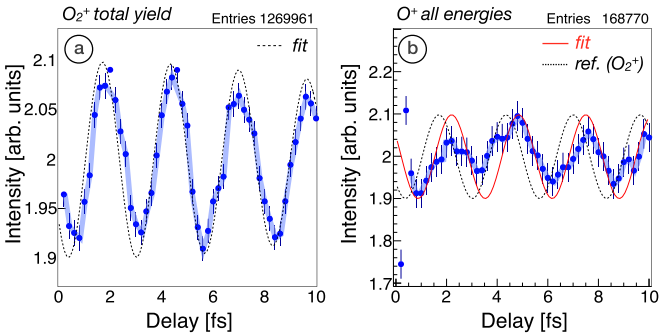

FIG. 7. Time-dependent ion yields with respect to the pump (XUV+IR)-probe (IR) delay. (a) Total O_2^+ ion yield, (b) total O^+ ion yield. A cosine fit to the O_2^+ ion yield is shown as a dashed line in (a) and (b). A cosine fit to the O^+ ion yield is shown as a solid line.

Applying the above-described technique of attosecond coherent control, this setup was used to manipulate the dissociation pathways of O_2^+ through quantum and optical interference of coherently excited states in the O_2^+ ion by changing the relative phase of the XUV pulse and the IR fields. The IR field was expected to cause a population transfer of the vibrational levels of the $B\,^2\Sigma_g^-$ state of O_2^+ to neighboring states or a quenching of the highest vibrational states by suppressing the barrier to direct dissociation. As shown in the previous static single pulse measurements (see Fig. 3), the high momentum resolution of this technique allows for a selection of specific electronic states or even vibrational levels by their energies, as well as by their transition geometry (i.e., their angular dependence), taking full advantage of the measured 3D momenta.

In contrast to the experiment by Siu *et al.* [12], the IR fields are present in the pump and probe pulses of the present experiments, producing a delay-dependent IR field intensity change. The IR probe pulse was delayed with respect to the XUV+IR pump pulse, which contains a broad range of photon energies: from ω, 3ω,5ω, and 7ω, up to 25ω. In addition, the XUV and IR fields were cross polarized, which influences the coupling of the electronic states populated by the XUV pulse in the presence of the IR field.

Figure 7 shows the total yield modulation of the O_2^+ (a) and O^+ (b) ions with respect to the pump-probe delay for ion kinetic

energies between 0 and 3.5 eV, averaged over all angles of dissociation. The O_2^+ yield shows an oscillation corresponding to the period ω of the infrared field of 2.7 fs. This effect is a manifestation of optical interference and is attributed to the strong-field enhanced ionization by the IR field, as well as the ionization caused by a combination of below-the-threshold harmonics for the ionization of O_2^+ (12.07 eV [25]) and the IR field. Adding a single IR photon to the Rydberg states populated by the below-the-threshold harmonics allows for an ionization to the $X\ ^2\Pi_g$ ground state of the O_2^+ ion. While these Rydberg states can be easily ionized by the total IR field the molecule is exposed to, at each delay step the modulation of the total IR intensity changes the probability for the one-photon absorption process. Thus, the time-dependent modulation of the total O_2^+ yield is an indicator of the absolute phase of the two IR fields. The O^+ ion yield, shown on the right, is also modulated with respect to the pump-probe delay. The oscillation, however, has a different phase with respect to the IR field, as indicated by a black dashed line. The modulation of the O^+ ion yield indicates the presence of additional frequencies in the signal. In the following discussion we will look at ways to differentiate these multiple contributions.

As discussed above, specific dissociation pathways lead to ion energies in a particular energy region. However, if multiple dissociation channels yield fragments that overlap in energy, a particular channel cannot be isolated by selecting a specific ion energy.

The probability of an electronic transition (or ionization), initiated by an XUV photon, depends on the molecular orientation with respect to the polarization axis of the electric field. For a parallel transition, no angular momentum along the axis is transferred to the electron. For a perpendicular transition, the transfer of angular momentum causes a different transition probability. Therefore, the strength by which the IR field couples two or more electronic states depends on the molecular orientation.

By choosing O^+ ions emitted at a particular angle with respect to the polarization axis, an electronic transition corresponding to a particular angular momentum transfer can be selected. This assumes that the axial recoil approximation holds, as the ion emission direction only corresponds to the orientation of the molecular axis at the instant of ionization if the dissociation is faster than the rotation of the molecule. For our ultrafast sub-10-fs transitions this is valid since any postalignment effects should not be important [37].

Energy- and angle-resolved O^+ yields are shown in Fig. 8. The delay dependent yield of O^+ ions is plotted for two different regions of O^+ ion kinetic energy, Fig. 8(a), 0.31–0.72 eV, and Fig. 8(b), 0.72–1.4 eV. The two regions are marked as B and C in the O^+ ion energy spectrum shown in Fig. 3. The data are further separated into O^+ ions emitted along the polarization axis of the XUV beam (red) and along the IR polarization axis (blue), as illustrated in the two top insets, depicting the orientation of the molecule with respect to the polarization vectors for both orientations. The molecular axes are allowed to deviate from a perfectly parallel orientation within a 37° cone in each case.

The highly differential energy and angle-selected data in Figs. 8(a) and 8(b) exhibit statistically significant oscillations with a varying phase relationship. We note here that the split-

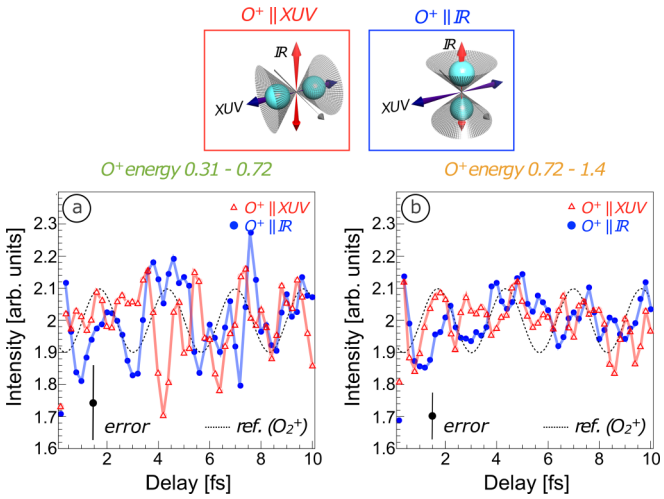

FIG. 8. Time-dependent O^+ ion yield from the ionization and subsequent dissociation of oxygen molecules in the pump-probe experiment. Pump: harmonics 3rd to 29th + IR; probe: IR. (a) O^+ ion yield with a kinetic energy of 0.31–0.72 eV (region B in Fig. 4) for ion emission along the XUV polarization direction, perpendicular to IR (red, triangle), and parallel to the infrared polarization axis (blue, dot), as indicated in the schematics on top. (b) The same but for an O^+ ion kinetic-energy range of 0.72–1.4 eV (region C in Fig. 4). The yields are averaged between adjacent bins. Colored semitransparent lines were added to guide the eye. The oscillating O_2^+ yield is represented by a dashed black wave to reference optical interference. The presented error bars are statistical and increase as we differentiate the data shown in Fig. 7.

mirror interferometer is intrinsically stable for performing the attosecond delay experiments. In the energy region shown in Fig. 8(a), ions emitted along the IR-polarization axis (blue) mostly follow the infrared field intensity at frequency ω. The phase of the optical interference is presented by the dash line, and is extracted from the total O_2^+ yield, as shown in Fig. 7(a). A different behavior is observed for the ions oriented along the XUV-polarization axis (red). At delays of ∼2–6 fs the yield oscillation is out of phase with respect to the IR intensity and then again mostly in phase with the IR field after 6 fs. Both oscillating intervals contain a higher frequency close to $2\,\omega$, suggesting that quantum interferences of electron wave packets play a significant role. For the energy region shown in Fig. 8(b), a similar behavior is observed, with a beating frequency faster than the IR frequency that is sometimes in phase and sometimes out of phase with the IR field.

The observed differences in the ionization yield for molecules parallel to the XUV or parallel to the IR polarization axes could correspond to the steering of the electronic states, initially populated by the XUV pulse, to different electronic states accessed by different angular momentum transfer to the molecule in the presence of the IR pulse. As outlined above, the angular restrictions suggest a selection of the following transitions: (i) (red) parallel XUV transition + perpendicular IR transition, (ii) (blue) perpendicular XUV transition + parallel IR transition.

In the experiment using solely the XUV radiation, as shown in Fig. 3, region (a) of Fig. 8 presents O^+ ions resulting from

the dissociation of the $3\,^2\Pi_u$ state as well as the autoionizing O_2^* states to the limit L3.

The $3\,^2\Pi_u$ state can be coupled by one infrared photon to the lower $B\,^2\Sigma_g^-$ state in a perpendicular transition and vice versa. A population transfer as well as quantum beating between the two states could therefore contribute to the observed oscillations. However, several other IR assisted transitions could produce O^+ ions in the same energy range. In the doublet system, the dissociation of the $A\,^2\Pi_u$ state could be enabled by the infrared field via the $1\,^2\Sigma_g^+$ state. In the quartet system, a two-photon transition from $b\,^4\Sigma_g^-$ to $2\,^4\Pi_g$ state leads to the dissociation to the L2 limit.

Optically allowed transitions between the $A\,^2\Pi_u$ and $B\,^2\Sigma_g^-$ states, as well as between the $b\,^4\Sigma_g^-$ and $c\,^4\Sigma_u^-$ states do not seem to match the photon energy in this experiment, or the number of photons required would lead to a parity violation. However, transitions involving other states as well as transitions driven by the absorption of more IR photons are likely to contribute to the observed yield oscillations.

The oscillations at the frequency of the IR driving field ω are a sign of intensity dependent population transfer or added population as a result of optical interference of the infrared field in both the pump and probe arms. Oscillations at a higher frequency are expected to be a result of quantum interferences between different pathways leading to dissociation. As shown above, multiple electronic states are coherently excited by the attosecond pulse train and various transitions are enabled by the infrared field. Thus, quantum interference of those pathways is expected and likely contributes to the observed oscillations. Phase shifts with respect to the driving field could also be a result of dynamics of the nuclei including the creation of new dissociation pathways by the infrared field. Due to the long IR pulse length of about 45 fs, nuclear dynamics in the bound states should be washed out by averaging over many cycles. However, the nuclear wave-packet motion in these states does influence the total dissociation yield after the XUV pulse has left; this results from the accumulated phase from the instant of the XUV ionization to the moment of resonant coupling of different electronic states by the IR field.

To investigate the physical origin of the oscillating O^+ ion yields of Fig. 8, we solved the time-dependent Schrödinger equation (TDSE) under the single active electron approximation. We solved the TDSE for O_2 molecules in a rectangle box with $192 \times 192 \times 512$ grids (and $r = 0.3$ a.u.) for all the valence orbits, and project out the wave function on to the Volkov states when the wave packet leaves the parent core (30–50 a.u.) [38]. We choose the XUV polarization direction as the z axis. We used an effective potential of O_2 molecules calculated from the generalized norm-conserving pseudopotentials [39] with a self-interaction correction [40,41]. Using pseudopotentials for dynamics of atoms in a strong field has been justified in Ref. [42]. The TDSE was solved on a rectangle box with equal space grid, which allows us to use fast Fourier transformation (FFT). When the IR laser pulse is over, we can obtain information on the dynamics, including the electron and ion kinetic-energy distributions and angular distributions.

In Fig. 9, we show the theoretical results that reproduce the main feature of the experimental data, as shown in Fig. 8: the yields for molecular orientations parallel to the XUV polarization (dashed lines) and parallel to the IR polarization (solid lines) are out of phase. In the calculations, we were averaging over all the electron energies and angles for a situation where the XUV pulse is polarized along the molecular axis (i.e., the z axis), and the IR pulse is perpendicular to the XUV pulse (i.e., see the top insets of Fig. 8). We note here that the theoretical treatment assumes a sudden coupling of the O_2 ground state with the highly excited O_2^{+*} states in the Franck-Condon region, and an additional coupling of these states by the IR pulse. Also, we note that the calculation does not take into account the nonequilibrium coupling of the electronic states as a function of the internuclear distance. Nevertheless, we observe that the yields for different orientations of the molecule are dephased, follow a full optical cycle periodicity, and have half-cycle modulations, as seen in the experiment and expected for the combination of the XUV and IR fields used here.

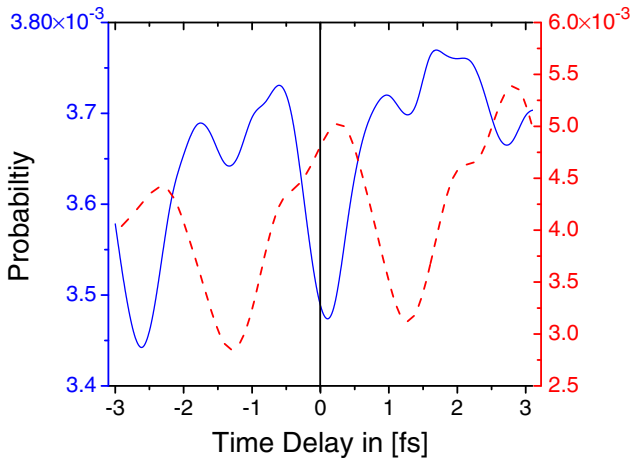

FIG. 9. Calculations of the time-dependent O^+ ion yields show periodic oscillations for different orientations of the molecular axis as a function of the delay between the XUV and IR pulses. In the calculation, we used the XUV intensity of 3.5×10^{10} W/cm^2. Because of the medium field strengths and the low Z of the oxygen target the spin-orbit approximation is valid, which allowed us to perform a spin-averaged simulation. Dashed (red) line (corresponding ordinate on the right): parallel orientation of the molecular axis and the XUV polarization. Solid (blue) line (corresponding ordinate on the left): molecular orientation parallel to the IR polarization. These yields are averaged over all electronic states.

In Fig. 10, we show the computed individual contributions of different electronic states that add to the total yield oscillations for the two orientations of the molecular axis and the IR and XUV fields, as shown in Fig. 9. For simplicity, we group all the electronic states as Π_g (depicted in blue), Π_u (depicted in red), and Σ states (depicted in black). Two striking features are immediately observable. First, the Σ states for both orientations of the molecular axis are oscillating with a half-optical cycle periodicity and their yield does not change. Second, the relative yield of the Π_g and Π_u states changes significantly.

Furthermore, the Π_u states oscillate following a full-optical-cycle periodicity, and are clearly out of phase, while the Π_g states show modulations of higher frequencies. These calculations suggest that the O_2^{+*} molecule dissociates through

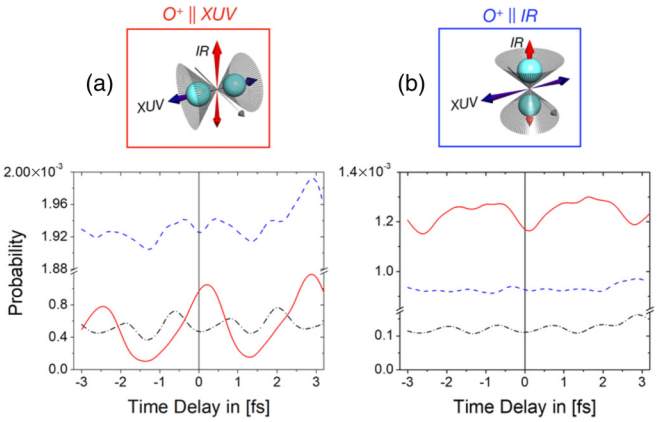

FIG. 10. State selective calculations of the time-dependent O^+ ion yields show a periodic oscillation for different orientations of the molecular axis as a function of the delay between the XUV and IR pulses. (a) parallel orientation of the molecular axis and the XUV polarization. (b) molecular orientation parallel to the IR polarization. Black (dot-dashed) lines: Σ states. Blue (dashed) lines: Π_g states. Red (solid) lines: Π_u states.

different channels as we vary the relative phase between the XUV and IR fields.

We see two major effects caused by the IR field. First, the total yield for different dissociation channels can be alternated by adding a relatively weak IR field to the XUV pulse, and second, attosecond coherent control can be added as a fine-tuning control knob of the dissociative process. Note that the population transfer of the electronic channels happens while the IR pulse is present, i.e., on a femtosecond time scale, while the predissociation process happens on a picosecond time scale.

Even in relatively simple highly excited molecules such as the states of O_2 excited in the present experiments, electron and nuclear wave-packet dynamics are highly correlated. To fully unravel the complex structure of the observed oscillations, advanced theoretical calculations are needed to disentangle such non-Born-Oppenheimer dynamics. From the experimental point of view, IR pulses as short as 5 fs would be necessary to better understand the role of the nuclear wave packet dynamics during the interaction of the XUV and IR pulses with the O_2^+ molecule. Such short IR pulses would help us to separate the IR pump and probe contributions and check whether optical and quantum interferences could be distinguished in the time domain. In the present experiment, the wide range of possible dynamics, as presented above, does not allow us to draw any further conclusions on the specific transitions and phase shifts at play. Using a multilayer XUV mirror, lower photon energies could be selected in order to populate fewer states in the dissociative ionization. Moreover, a coincident measurement of the electron energy would clearly help us to better unravel the many transitions involved. The measurements presented here showcase the possibilities to study nuclear and electron interaction with quantum control techniques in combination with a momentum imaging setup.

IV. CONCLUSION

In the experiments and calculations presented in this work, attosecond pulse trains were used to highly excite molecular oxygen cations. The subsequent dissociation was measured by means of high resolution 3D ion momentum imaging and manipulated by adding an IR field. We have used the inherent sub-optical-cycle resolution (∼170 as) of our pump-probe delay stage to coherently control dissociative ionization processes in oxygen molecules (O_2^{+*}) by means of the attosecond XUV frequency comb and the femtosecond infrared field. First, we spectrally postselected the contributions from the 11th, 13th, and 15th harmonics in the momentum-space analysis to coherently populate several bound electronic states of O_2^{+*} that predissociate through nonadiabatic state coupling to multiple dissociation limits on a picosecond time scale. Then, we used an IR pulse to coherently switch the population of different electronic states, thus, manipulating the dissociation process on an attosecond time scale.

Due to the rapid dissociation processes enabled through nonadiabatic couplings, electron wave-packet interferences are strongly coupled with nuclear wave-packet dynamics, rendering theoretical calculations particularly challenging, even in a simple linear molecule such as O_2. Taking advantage of the high-resolution 3D ion momentum imaging spectrometer coupled with attosecond XUV pulse trains and femtosecond IR pulses, these experiments show that electron wave-packet interferometry involving non-Born-Oppenheimer dynamics can be performed with high-energy resolution to identify adjacent vibrational levels of highly excited O_2^{+*} ions.

We showed that the IR field, working in combination with the XUV pulses, can be used to rearrange the distribution of the excited electronic states, which influences how the molecule dissociates long after the XUV and IR pulses are gone. The results suggest that it could be beneficial to use a stronger IR field to control the dissociation process via tunnel ionization of the bound states during the interaction of the IR field with the molecule. In such a case, the predissociation process would be abruptly interrupted by the strong IR field. The signature of such an interaction could manifest itself in a broadening of the O^+ ion energy peaks of the vibrational states, which could be well resolved using the high-resolution 3D momentum imaging technique.

ACKNOWLEDGMENTS

We acknowledge many fruitful discussions and advice from R. Dörner, M. S. Schöffler, and L. Ph. Schmidt. We are indebted to O. Jagutzki and A. Czasch from Roentdek GmbH and T. Jahnke from Cronologic GmbH for outstanding support for their momentum imaging detectors, readout, and software. C. Khurmi, J. Cryan, and E. Champenois gave valuable support with the laser system. F.S. acknowledges financial support by Studienstiftung des deutschen Volkes. This work was supported by the Director, Office of Science, Office of Basic Energy Sciences, and by the Division of Chemical Sciences, Geosciences, and Biosciences of the U.S. Department of Energy at LBNL under Contract No. DE-AC02-05CH11231. X.M.T. was supported by a Grants-in-Aid for

Scientific Research (Grant No. JP16K05495) from the Japan Society for the Promotion of Science. TDSE calculations were performed using supercomputer (COMA) at Center for Computational Sciences, University of Tsukuba, Japan.

[1] A. H. Zewail, J. Phys. Chem. A **104**, 5660 (2000).
[2] A. S. Alnaser, B. Ulrich, X. M. Tong, I. V. Litvinyuk, C. M. Maharjan, P. Ranitovic, T. Osipov, R. Ali, S. Ghimire, Z. Chang, C. D. Lin, and C. L. Cocke, Phys. Rev. A **72**, 030702 (2005).
[3] M. Drescher, M. Hentschel, R. Kienberger, M. Uiberacker, V. Yakovlev, A. Scrinzi, T. Westerwalbesloh, U. Kleineberg, U. Heinzmann, and F. Krausz, Nature (London) **419**, 803 (2002).
[4] M. Uiberacker, T. Uphues, M. Schultze, A. J. Verhoef, V. Yakovlev, M. F. Kling, J. Rauschenberger, N. M. Kabachnik, H. Schröder, M. Lezius, K. L. Kompa, H.-G. Muller, M. J. J. Vrakking, S. Hendel, U. Kleineberg, U. Heinzmann, M. Drescher, and F. Krausz, Nature (London) **446**, 627 (2007).
[5] P. Johnsson, J. Mauritsson, T. Remetter, A. L'Huillier, and K. J. Schafer, Phys. Rev. Lett. **99**, 233001 (2007).
[6] P. Ranitovic, X. M. Tong, B. Gramkow, S. De, B. DePaola, K. P. Singh, W. Cao, M. Magrakvelidze, D. Ray, I. Bocharova, H Mashiko, A. Sandhu, E. Gagnon, M. M. Murnane, H. C. Kapteyn, I. Litvinyuk, and C. L. Cocke, New J. Phys. **12**, 013008 (2010).
[7] P. Brumer and M. Shapiro, Chem. Phys. Lett. **126**, 541 (1986).
[8] V. Blanchet, C. Nicole, M.-A. Bouchene, and B. Girard, Phys. Rev. Lett. **78**, 2716 (1997).
[9] R. J. Gordon, L. Zhu, and T. Seideman, J. Phys. Chem. A **105**, 4387 (2001).
[10] P. Ranitovic, X. M. Tong, C. W. Hogle, X. Zhou, Y. Liu, N. Toshima, M. M. Murnane, and H. C. Kapteyn, Phys. Rev. Lett. **106**, 193008 (2011).
[11] C. W. Hogle, X. M. Tong, L. Martin, M. M. Murnane, H. C. Kapteyn, and P. Ranitovic, Phys. Rev. Lett. **115**, 173004 (2015).
[12] W. Siu, F. Kelkensberg, G. Gademann, A. Rouzée, P. Johnsson, D. Dowek, M. Lucchini, F. Calegari, U. De Giovannini, A. Rubio, R. R. Lucchese, H. Kono, F. Lépine, and M. J. J. Vrakking, Phys. Rev. A **84**, 063412 (2011).
[13] P. Ranitovic, C. W. Hogle, P. Rivière, A. Palacios, X.-M. Tong, N. Toshima, A. G. Castrillo, L. Martin, F. Martín, M. M. Murnane, and H. Kapteyn, Proc. Natl. Acad. Sci. USA **111**, 912 (2014).
[14] C. Guo, M. Li, J. P. Nibarger, and G. N. Gibson, Phys. Rev. A **58**, R4271 (1998).
[15] A. M. Sayler, P. Q. Wang, K. D. Carnes, B. D. Esry, and I. Ben-Itzhak, Phys. Rev. A **75**, 063420 (2007).
[16] S. De, M. Magrakvelidze, I. A. Bocharova, D. Ray, W. Cao, I. Znakovskaya, H. Li, Z. Wang, G. Laurent, U. Thumm, M. F. Kling, I. V. Litvinyuk, I. Ben-Itzhak, and C. L. Cocke, Phys. Rev. A **84**, 043410 (2011).
[17] Q. Song, Z. Li, H. Li, P. Lu, X. Gong, Q. Ji, K. Lin, W. Zhang, J. Ma, H. Zeng, F. He, and J. Wu, Opt. Express **25**, 2221 (2017).
[18] K. P. Singh, F. He, P. Ranitovic, W. Cao, S. De, D. Ray, S. Chen, U. Thumm, A. Becker, M. M. Murnane, H. C. Kapteyn, I. V. Litvinyuk, and C. L. Cocke, Phys. Rev. Lett. **104**, 023001 (2010).
[19] F. Kelkensberg, W. Siu, J. F. Pérez-Torres, F. Morales, G. Gademann, A. Rouzée, P. Johnsson, M. Lucchini, F. Calegari, J. L. Sanz-Vicario, F. Martín, and M. J. J. Vrakking, Phys. Rev. Lett. **107**, 043002 (2011).
[20] H. Timmers, N. Shivaram, and A. Sandhu, Phys. Rev. Lett. **109**, 173001 (2012).
[21] P. Cörlin, A. Fischer, M. Schönwald, A. Sperl, T. Mizuno, U. Thumm, T. Pfeifer, and R. Moshammer, Phys. Rev. A **91**, 043415 (2015).
[22] RoentDek, RoentDek Handels GmbH (2015).
[23] F. P. Sturm, T. W. Wright, D. Ray, I. Zalyubovskaya, N. Shivaram, D. S. Slaughter, P. Ranitovic, A. Belkacem, and T. Weber, Rev. Sci. Instrum. **87**, 063110 (2016).
[24] A. A. Wills, A. A. Cafolla, and J. Comer, J. Phys. B: At., Mol. Opt. Phys. **24**, 3989 (1991).
[25] P. Baltzer, B. Wannberg, L. Karlsson, M. C. Göthe, and M. Larsson, Phys. Rev. A **45**, 4374 (1992).
[26] Y. Lu, Z. He, J. Cutler, S. Southworth, W. Stolte, and J. Samson, J. Electron Spectrosc. Relat. Phenom. **94**, 135 (1998).
[27] M. Richard-Viard, O. Dutuit, M. Lavollée, T. Govers, P. M. Guyon, and J. Durup, J. Chem. Phys. **82**, 4054 (1985).
[28] T. Akahori, Y. Morioka, M. Watanabe, T. Hayaishi, K. Ito, and M. Nakamura, J. Phys. B: At. Mol. Phys. **18**, 2219 (1985).
[29] A. Lafosse, J. C. Brenot, A. V. Golovin, P. M. Guyon, K. Hoejrup, J. C. Houver, M. Lebech, and D. Dowek, J. Chem. Phys. **114**, 6605 (2001).
[30] A. Lafosse, J. C. Brenot, P. M. Guyon, J. C. Houver, A. V. Golovin, M. Lebech, D. Dowek, P. Lin, and R. R. Lucchese, J. Chem. Phys. **117**, 8368 (2002).
[31] F. Merkt, P. M. Guyon, and J. Hepburn, Chem. Phys. **173**, 479 (1993).
[32] M. Magrakvelidze, C. M. Aikens, and U. Thumm, Phys. Rev. A **86**, 023402 (2012).
[33] F. P. Sturm, X. M. Tong, A. Palacios, T. W. Wright, I. Zalyubovskaya, D. Ray, N. Shivaram, F. Martín, A. Belkacem, P. Ranitovic, and T. Weber, Phys. Rev. A **95**, 012501 (2017).
[34] R. I. Hall, G. Dawber, A. McConkey, M. A. MacDonald, and G. C. King, Phys. Rev. Lett. **68**, 2751 (1992).
[35] R. Feifel, J. H. D. Eland, and D. Edvardsson, J. Chem. Phys. **122**, 144308 (2005).
[36] N. Shivaram, H. Timmers, X.-M. Tong, and A. Sandhu, Phys. Rev. Lett. **108**, 193002 (2012).
[37] X. M. Tong, Z. X. Zhao, A. S. Alnaser, S. Voss, C. L. Cocke and C. D. Lin, J. Phys. B: At., Mol. Opt. Phys. **38**, 333 (2005).
[38] X. M. Tong, K. Hino, and N. Toshima, Phys. Rev. A **74**, 031405(R) (2006).
[39] D. R. Hamann, Phys. Rev. B **40**, 2980 (1989).
[40] X.-M. Tong and S.-I. Chu, Phys. Rev. A **55**, 3406 (1997).
[41] X. Chu and S.-I. Chu, Phys. Rev. A **63**, 023411 (2001).
[42] X.-M. Tong, G. Wachter, S. A. Sato, C. Lemell, K. Yabana, and J. Burgdörfer, Phys. Rev. A **92**, 043422 (2015).